論 文

Improvement of Oxidation Resistance of Gray Cast Iron with Thermal Sprayed Silicon Coating by Laser Surface Alloying

Heung-il Park and Kazuhiro Nakata*

요 약

회주철 모재의 표면에 감압 플라즈마 용사법으로 실리콘 분말을 피복시킨 후 CO_2 레이저를 이용하는 표면 합금화로 고온 내스케일성이 향상된 표면 개질층을 제조하였다. 실리콘의 표면 합금층에는 응집상의 흑연(chunky graphite)이 Fe_5Si_3로 구성된 망상의 화합물 기지속에 정출하는 조직특성을 보였다. 대기 분위기에서 18.0ks 동안 열중량측정(TG)한 결과 실리콘 표면 합금층의 무게 증가율은 회주철 모재에 비하여 923K에서는 약 1/3, 1098K에서는 약 1/10을 나타내었다. 그리고 1098K에서 18.0ks 동안 유지시킨 주철모재 시편에서 원래의 모재표면을 기준으로 다공성의 외부스케일과 편상흑연을 따라 생성된 내부스케일로 구성된 두께 60~70 μm의 두꺼운 산화스케일이 생성되었으나, 실리콘의 표면 합금층에서는 두께 3~5 μm의 치밀한 외부 산화스케일만이 생성되었다. 실리콘 합금층의 단면 미소경도값은 MHV 300~1100으로 그 변동폭이 심하였으나, 진공분위기에서 열처리(1223K, 18.0ks)한 경우 미소경도값의 편차는 MHV 300~500으로 개선되었다.

(Received July 14, 1998)

1. Introduction

A laser surface treatment is carried out to improve oxidation, corrosion, and wear resistant properties of materials by altering alloy compositions and microstructural features of a surface of substrate material [1, 2]. Among several forms of laser processing of materials, laser surface alloying is the process which locally modifies the surface of inexpensive substrate by adding small quantities of alloying elements to a molten metal pool generated by intense laser irradiation [3-5].

The advantages of cast iron as engineering material are that the cast iron can be used to produce complex shaped parts economically because of good castability and it has good machinability and lubrication property [6]. In general, previous research works on the laser processing of the cast iron can be divided into three categories, that is, the transformation hardening process such as hard eye treatment of the cast iron [7], and hardening of a cylinder liner [8] and a piston ring [9] for a diesel engine, the surface melting process for a cam shaft and a rocker arm [10, 11], and surface alloying process for a valve seat [8]. These processes were intended to improve the wear resistance of the cast iron surface using carbon contained sufficiently in the cast iron matrix.

The flake iron Silal which contained 4 to 6 mass% silicon was one of the earliest heat resisting alloys developed [12]. Silicon is a essential alloying element as graphitizer in cast iron. Silicon addition of 3.5 to 7 mass% improves high-temperature properties of the cast iron by raising eutectoid transformation temperature [13]. Elevated levels of silicon also reduce the rate of scaling and growth by forming a tight, adhering oxide scale. Moreover the silicon addition of 14 to 17 mass% yields cast iron improves significantly to resistance corrosive acids [13]. Therfore increasing silicon content in the cast iron, increases not only the heat resistance but also acid resistance, however, elongation and toughness decrease dramatically, and workability and castability are degraded by the precipitation of Kishy graphite or η phase [14, 15]. Surface alloying of silicon on a low alloy cast iron part manufactured by a near net shape is a potential process to improve the heat and acid resistances without degradation of mechanical properties of the bulk cast iron and to minimize casting defects.

In this study, the surface modification to producing

부경대학교 생산가공공학과(Deprt. of Production and Joining Eng., Pukyong National University, 608-739)
*오사카대학 접합과학연구소(Joining and Welding Research Institute, Osaka University, Osaka, 567, Japan)

high temperature oxidation resistant layer on the surface of the cast iron by laser alloying silicon, which is typical alloying element of the cast iron, was investigated. A CW CO_2 laser was used to form silicon alloyed layer on the cast iron surface by remelting a pure silicon layer precoated by low pressure plasma spraying. The effect of laser beam traveling speed on the macrostructure and microstructure of the silicon alloyed layer was examined and high temperature oxidation behavior was investigated.

2. Experimental procedure

The chemical composition of gray cast iron used in this study and the size and the chemical composition of silicon powder are shown in Table 1. Flake graphite cast iron was poured into a green sand mold in the dimension of 100×120×10 mm and machined to a plate in the dimension of 50×60×6 mm. A surface of the machined plate was cleaned with aceton and was blasted by alumina powder to improve bonding strength of thermal sprayed coating. Spray powder was commercial grade (Powrex Ltd.) and had the size distribution of −63~+10 μm (Fig. 1a).

The conditions of low pressure plasma spraying and surface alloying by CW CO_2 laser processing are shown in Table 2. Specimen designation was GXX and GSXX, where G referred to a gray cast iron substrate without silicon coating, GS referred the silicon coated specimens and XX referred the traveling speed of the laser beam. To obtain a dense coating and minimize oxidation of silicon powder during thermal spraying, plasma sprayer (METECO 7MB, 80kW) was used under the low pressure atmosphere of 2.67× 10^4Pa. Argon and hydrogen gases were used as primary and secondary gases, respectively. Thus,

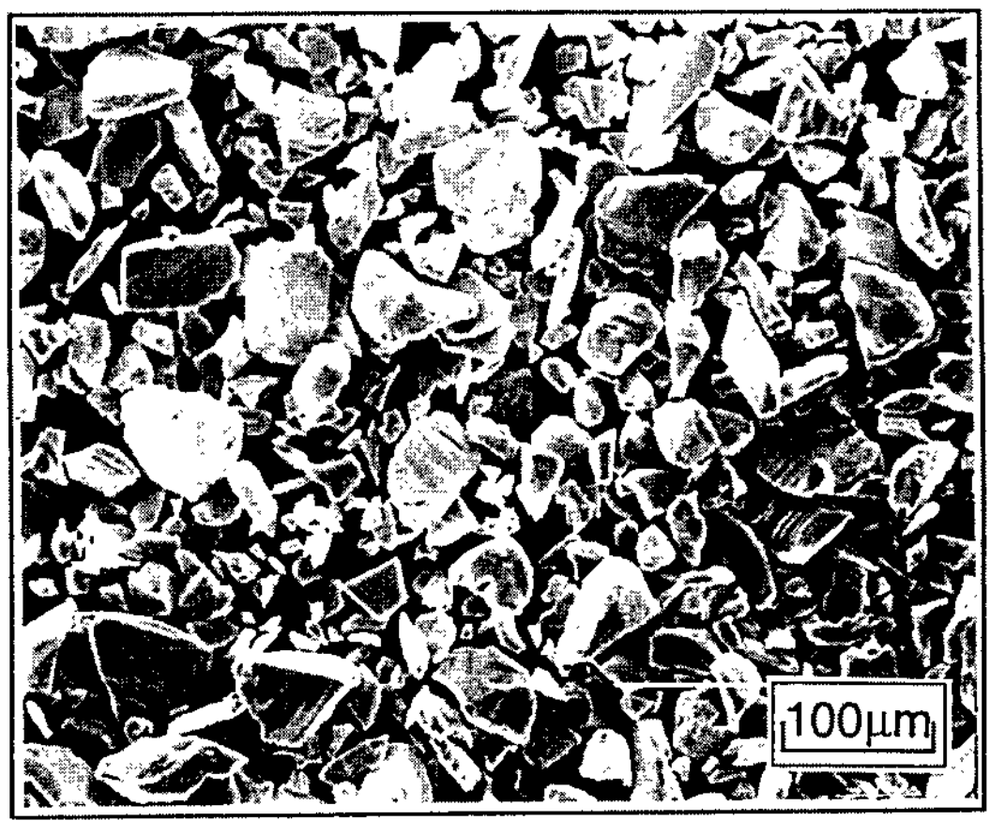

Fig. 1. Scanning elecron micrographs of (a) silicon powder and (b) plasma sprayed silicon coating on the gray cast iron.

silicon precoat of 150 μm in thickness was formed on the plate without peeling and cracking (Fig. 1b).

The surface alloying of silicon was carried out using CW CO_2 laser (MITSUBISHI 25C) at the condition of the laser output of 2300W. A defocused beam of 1mm in diameter on the surface at a frocus position of 50mm upwards from the specimen surface

Table 1. Chemical compositions of materials

Materials	Chemical compositions, wt.%								Remarks
	C	Si	Mn	P	S	Al	Ca	Fe	
Base metal	3.4	1.8	0.8	0.08	0.08	–	–	Bal.	Casting dimension: 100×120×10 (mm) Specimen dimension: 50×60×6 (mm)
Silicon powder	0.007	Bal.	<0.01	–	0.001	0.01	<0.01	0.16	Commercial grade (Powrex Ltd.) Grain size: +63~−10 μm

Table 2. Conditions of low pressure plasma spraying and laser surface alloying

Low pressure plasma spraying	
Pressure (Pa)	2.67×10^4
Primary gas	Ar
Pressure (Pa)	1.3×10^4
Flow rate (m^3/s)	8.0×10^{-4}
Secondary gas	H_2
Pressure (Pa)	1.20×10^4
Flow rate (m^3/s)	1.44×10^{-4}
Plasma conditions	
Arc current (A)	600
Arc voltage (V)	55
Spraying distance (mm)	250

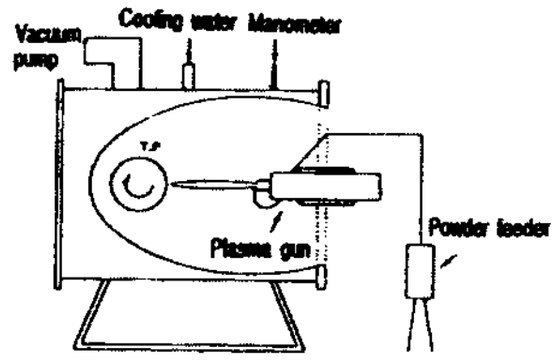

Plasma gun : METECO 7MB

Laser surface alloying	
Power (W)	2300 (multi mode)
Traveling speed (mm/s)	0.83, 1.67, 3.33, 5.00
Defocused distance (mm)	+50
Scanning frequency (Hz)	100
Scanning width (mm)	5
Shield gas	Ar

Specimen symbols

Groups	Traveling speeds (mm/s)			
	0.83	1.67	3.33	5.00
Base metal	G50	G100	G200	G300
Si-coated	GS50	GS100	GS200	GS300

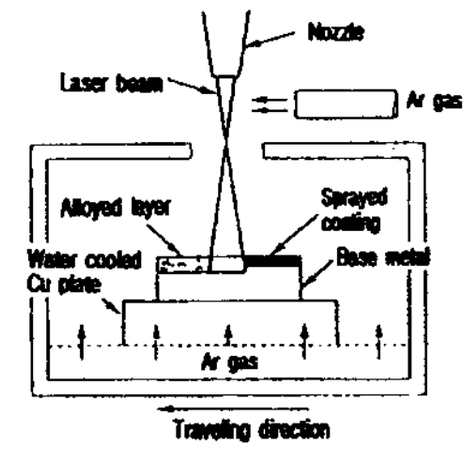

CO_2 laser : MITSUBISHI 25C

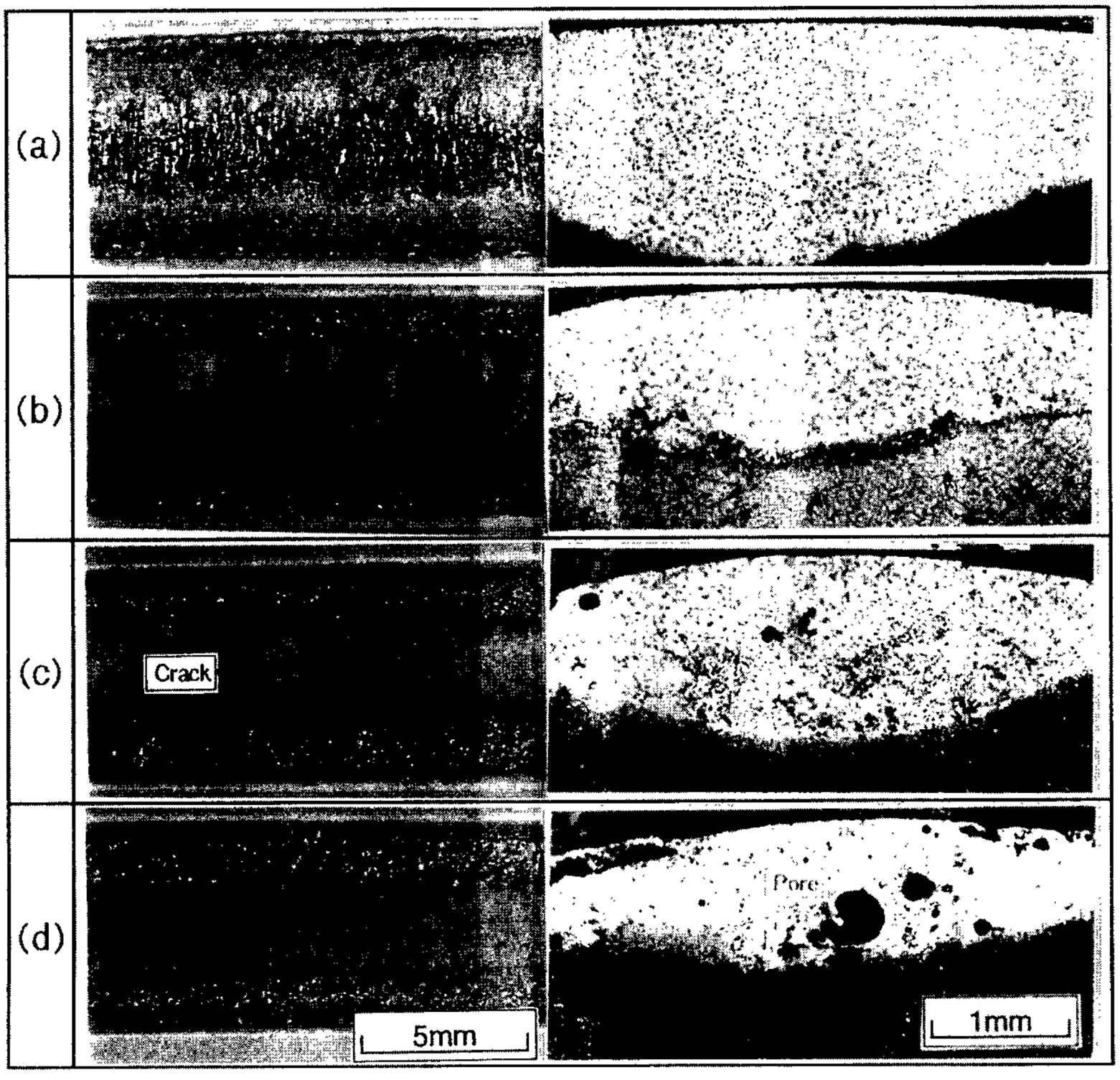

Fig. 2. Surface appearence and cross-sectional microstructures of as-laser alloyed bead at the various traveling speed of laser beam. (a) 0.83 mm/s (GS50), (b) 1.67 mm/s (GS100), (c) 3.33 mm/s (GS200) and (d) 5.0 mm/s (GS300).

(deforcusing distance +50 mm) was used mainly to prevent plasma formation, and partly to get smooth bead surface. To get wide bead width and homogeneous alloyed bead, beam scanning was also used at scanning width of 5 mm with scanning frequency of 100Hz. The single bead of 50 mm in length was produced in the argon gas atmosphere with the various laser beam traveling speeds of 0.83, 1.67, 3.33 and 5.00 mm/s. To dissolve cementite formed by the laser treatment, the surface alloyed specimen was heat treated under a vacuum furnace (6.7×10^{-3}Pa, 1223K, 18.0ks) and furnace cooled. Microstructures were observed using an optical microscope and a scanning electron microscope (SEM), and electron probe microanalysis (EPMA), and X-ray diffraction analysis (XRD) were done to measure the alloying element distribution and phase identification, respectively, and microhardness testing were performed. Oxidation resistance of the alloyed layer was measured by thermogravimetric analysis (TGA) at the isothermal condition of 923 and 1098K, respectively, in the air up to 18.0ks.

3. Results and discussions

3.1 Macrostructures of silicon alloyed bead sections

The cross-sectional structures of silicon alloyed bead at the various traveling speeds of laser beam are shown in Fig. 2. The surface of alloyed bead was relatively flat. The microstructure of bead section showed that fine granular graphites were precipitated in the alloyed layer but ledeburites were not obseved. This indicated that the precipitation of graphite is possible by the surface alloying of silicon under the non-equilibrium solidification condition where the cooling rate of bead is faster than 1×10^{4}K/s, which was estimated by the relationship between cooling rate and dendrite arm spacing of ledeburite [16]. However, gas pores were obseved as the traveling speed of laser beam was faster than 3.33 mm/s (GS200).

The gas pores generated in the bead are possibly introduced by the {CO} gas. The gas can be generated by the reduction of $<SiO_2>$ with the carbon. $<SiO_2>$ is formed by the [O] introduced from the atmosphere or suspended on the cast iron matrix [17]. In the case of GSXX which had the same coat thickness of 150 μm, the content of silicon is increased in the silicon alloyed layer as the travelling speed increased because the fusion amount of base metal decreased [18]. As [Si] increases, equilibrium constant, K ($=[Si]/[C]^2$), of reaction, $<SiO_2>+2[C]=[Si]+2\{CO\}$, increases. This makes the temperature range of $<SiO_2>$ formation wide and then the amount of {CO} gas generation increases in the bead [19]. Therefore, the gas pores were trapped in the bead of GS200 and GS300 were produced by the increased amount of {CO} gas as the silicon content increased in the bead due to the decrease in the fusion amount of base metal. In addition, increasing solidification rate of weld pool as increasing traveling speed prevented the gas pore to escape from the molten pool surface.

The changes of width and melt depth of bead in GXX and GSXX at the various traveling speeds of laser beam are shown in Fig. 3. As the traveling speed increased, both melt depth and width of the bead decreased due to decreased heat input to the bead at constant laser output, and the Si-coated specimen showed larger values in the melt depth and width of bead than the as-blasted base metal specimen at each

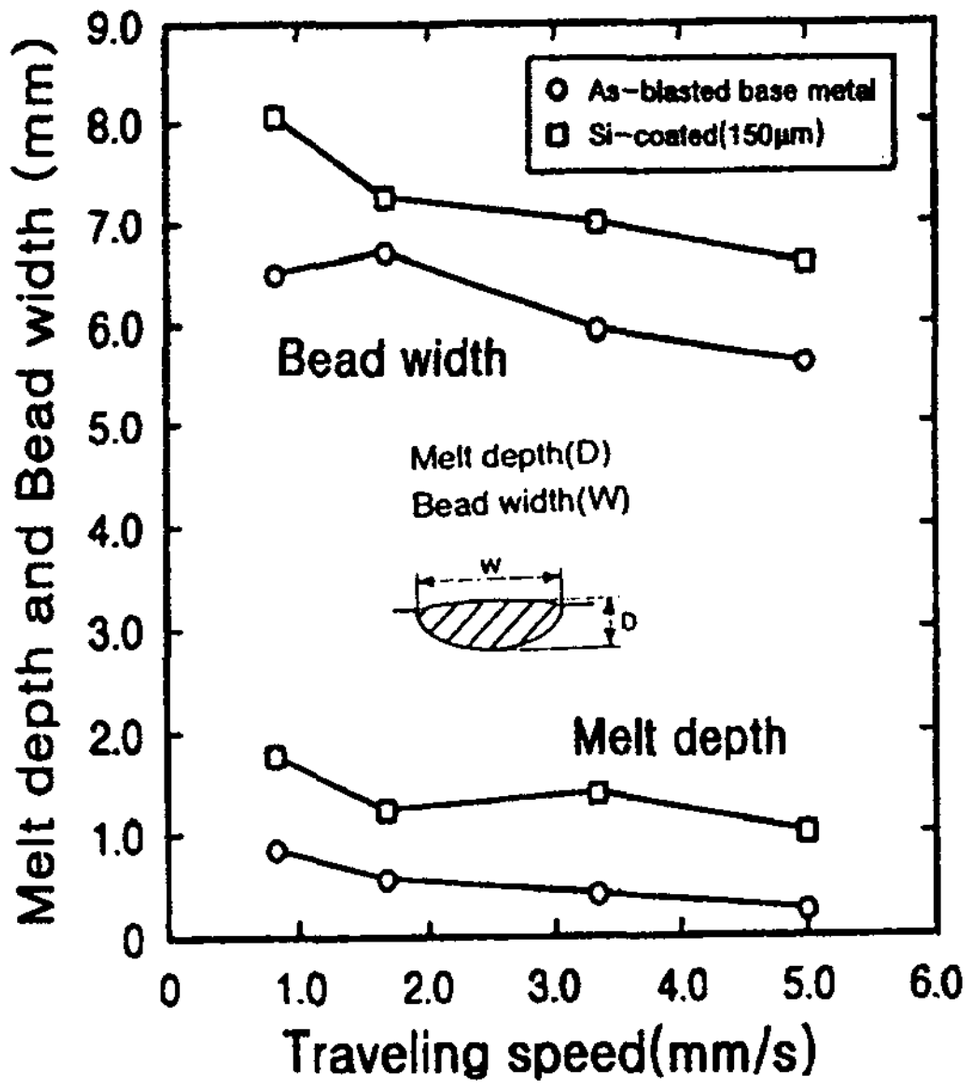

Fig. 3. Effects of silicon coating and traveling speeds on the bead width and melt depth.

traveling speed. These increases in the width and the melt depth of bead due to the silicon coating is attributed to the increase of absoption rate of laser energy by the silicon coating [20] and the decrease of melting point in the cast iron by the silicon alloying [21]. In fact, when as-blasted base metal was remelted by laser severe reflection of laser beam and lenz contamination were observed.

3.2 Solidification microstructure of silicon alloyed layer

The optical microstructure of silicon alloyed layer as laser-alloyed condition was devided into two zones, a fusion zone (FZ) where fine granular graphites were precipitated and HAZ as shown in Fig. 4a, in higher magnification of Fig. 2a. In the weld of general cast iron, a ledeburite zone is clearly observed between FZ and HAZ [22]. However, the ledeburite zone was not clearly showed on the silicon alloyed layer due to silicon effect as graphitizer in the molten pool [26].

A typical SEM micrograph of solidification microstructure in the FZ of silicon alloyed layer in GS 50 etched with HNO_3+HF+H_2O solution is shown in Fig. 4b. Fig. 4b is from a middle part of alloyed bead

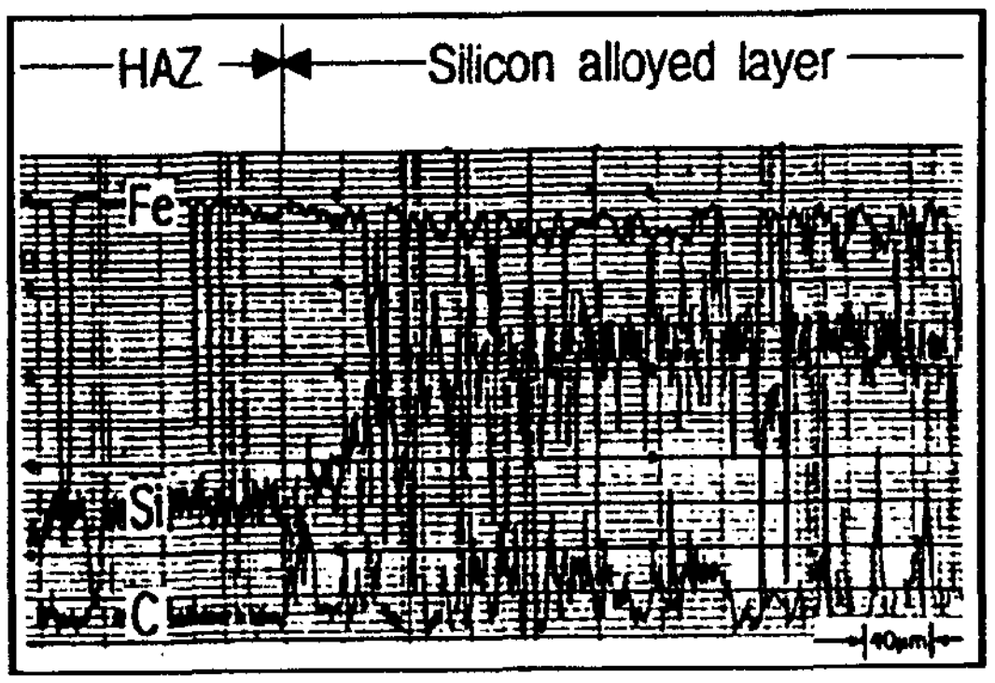

Fig. 5. EPMA profile of iron, silicon and carbon for the silicon alloyed bead section in GS50 (see Fig. 4a).

with large amount of intermetallic compounds. Chunky graphites in the size of 20 μm where the growth was limited severely were precipitated in the ferrite matrix and network compounds were observed in the eutectic cell boundary. Ferrite matrix around the chunky graphites was etched out and the network compound in the eutectic cell boundary was not etched.

Fig. 5 shows the concentation profile on the elements of iron, silicon and carbon in the same bead of GS50 by EPMA. In FZ where fine granular graphites were precipitated, the concentration of silicon

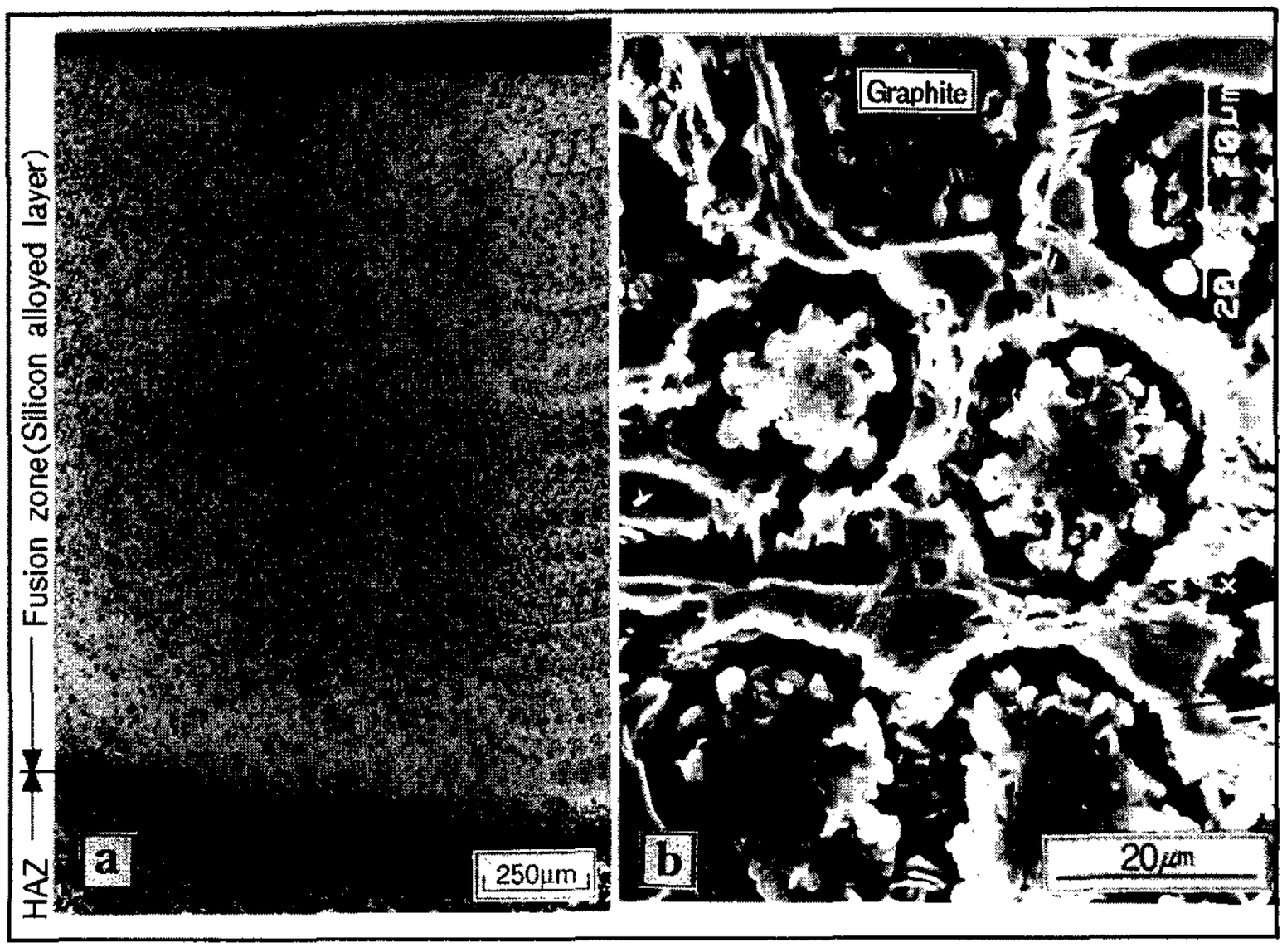

Fig. 4. Optical and scanning electron micrographs of sillicon alloyed layer in GS50, as-laser alloyed.
(a) silicon alloyed bead section etched with 4% nital. (b) middle part of alloyed layer in fig. 4(a) etched with HNO_3+HF+H_2O solution.

was high by laser surface alloying. There existed a limited mixing zone of silicon (see Fig. 4a) where the concentration of silicon was gradually decreased and had a narrow width of about 100 μm between the FZ and HAZ. In general, the ledeburite zone observed in the cast iron weld corresponds to the area where filler material is not mixed because remelting of matrix adjacent to the melt boundary is proceeded during solidification of weld pool [22]. The fact that there was no ledeburite zone in silicon alloyed layer is presumably because the homogenization of alloying elements is achieved easily throughout the fusion zone due to the convective motion of weld pool [3] and an increased fluidity of molten metal by silicon alloying.

Fig. 6 is the result of X-ray diffraction analysis on the silicon alloyed layer of GS50 and shows that the matrix consists of α-Fe, Fe_3C and Fe_5Si_3. From above results, the solidification microstructure of silicon alloyed layer consisted of the chunky graphites precipitated in the ferrite matrix and network shaped Fe_5Si_3 compound obserbed in the eutectic cell boundary.

During melting and mixing of silicon coat together with the base metal by laser irradiation, unresolved flake graphite fragments can act heterogeneous nucleation sites for graphite [23]. Once graphite has nucleated, the eutectic cell grows in an approximately radial manner within the constraints imposed by surrounding austenite dendrites. The growth of graphite is controlled by the diffusion of carbon [24]. In addition, as increasing the amount of silicon to liquid iron, carbon supply by diffusion is boosted due to the decrease of carbon solubility [25]. As silicon is a strong graphitizer, increasing silicon content on the liquid iron increased a carbon equivalent, and thus the formation of chill is suppressed due to the increased temperature interval between iron-graphite eutectic temperature and iron-carbide eutectic temperature of liquid metal [26]. From the above discussions, the suppression of the chill formation in the whole section of the silicon alloyed layer even with the rapid cooling of bead faster than 1×10^4K/s is attributed to the graphitization effect of silicon and to the inhibition of

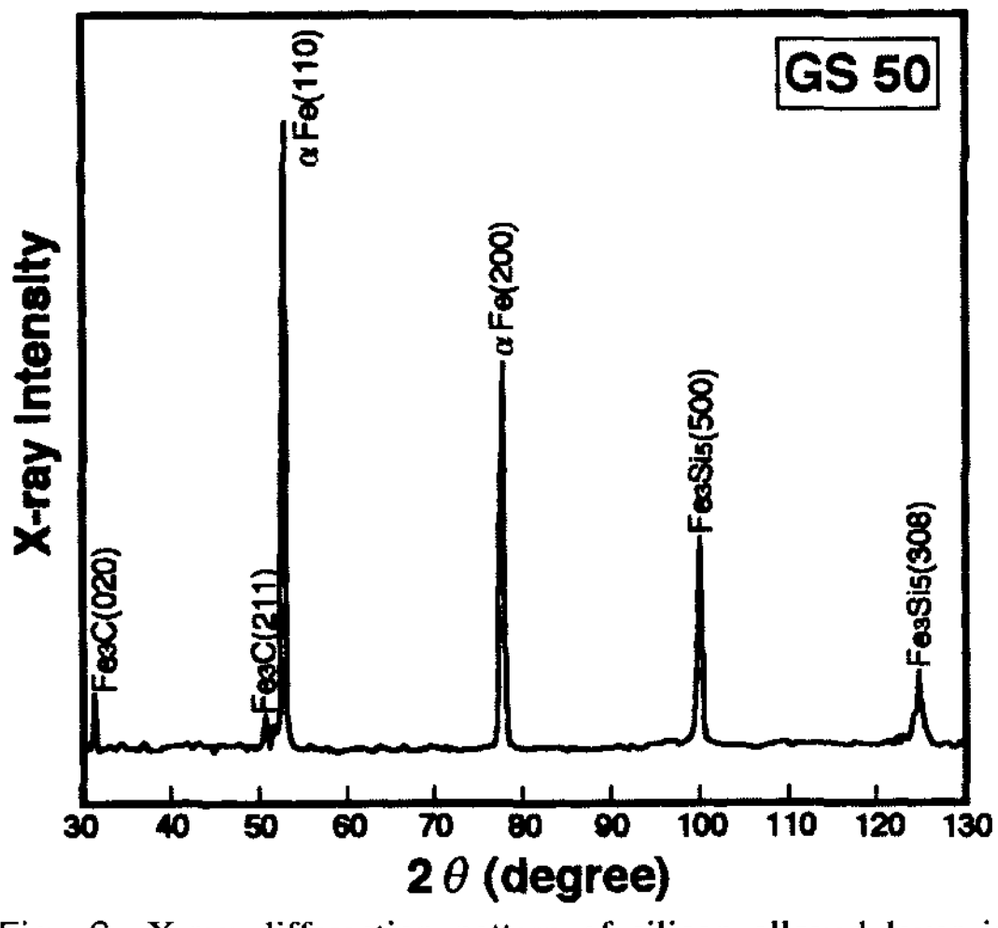

Fig. 6. X-ray differaction pattern of silicon alloyed layer in GS50, as-laser alloyed.

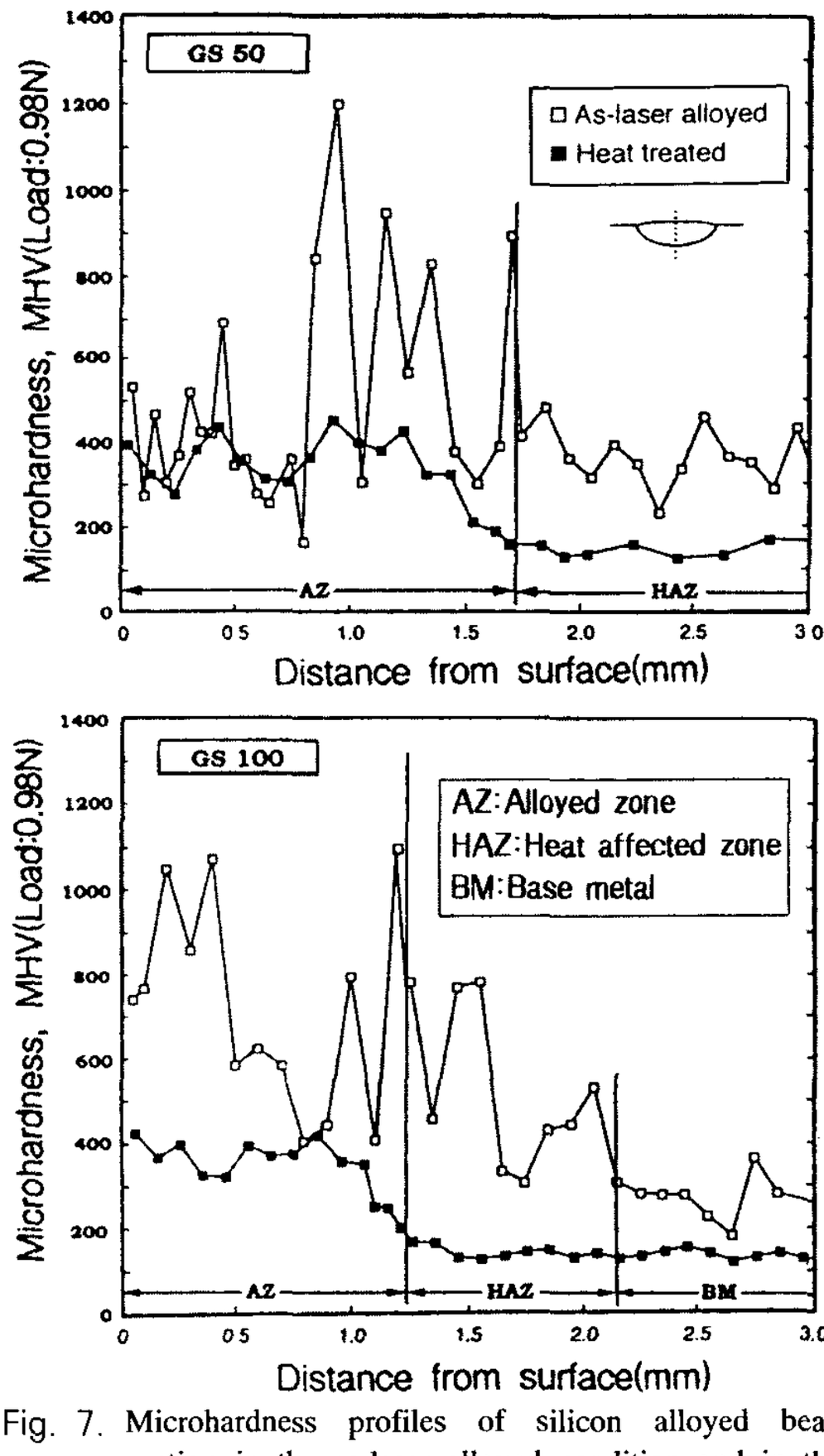

Fig. 7. Microhardness profiles of silicon alloyed bead section in the as-laser alloyed condition and in the post heat-treated condition. (a) GS50 and (b) GS100.

eutectic cell growth due to the network segregation of Fe_5Si_3 compounds.

3.3 Hardness profile of silicon alloyed layer

Fig. 7 shows the microhardnesses of bead sections in GS50 and GS100, compared to those of the specimen heat treated to decompose cementite in the silicon alloyed layer. In GS50 the microhardness of the bead surface which is a finally solidified area was MHV 300~500, and that of the center of bead increased to MHV 600~900. On the other hand, the microhardness in the bead surface was MHV 800~1100 while that of the bead center was decreased to MHV 400~700 in GS100. However, after post heat treatment at 1223K for 18.0ks in vacuum and furnace cooled, the microhardnesses of both the bead surface and the center were decreased to MHV 300~500. It seems that the reason of these irregular hardness distribution depends upon the amount of graphite and Fe_5Si_3 compounds formed in the matrix across the bead section as shown in Fig. 4. The decreased microhardness of the alloyed layer after post heat treatment is attributed to decomposition of cementite in the matrix to ferrite and temper carbon.

3.4 High temperature oxidation behavior of silicon alloyed layer

Fig. 8a shows a high temperature oxidation behavior in the silicon alloyed layer at 1098K in the air. Oxidation scale in the base metal as shown in Fig. 8b consisted of a layer of porous external scale grown to the outside from the original surface of the base metal and a layer of internal scale grown along flake graphites inside the matrix. The total thickness of external and

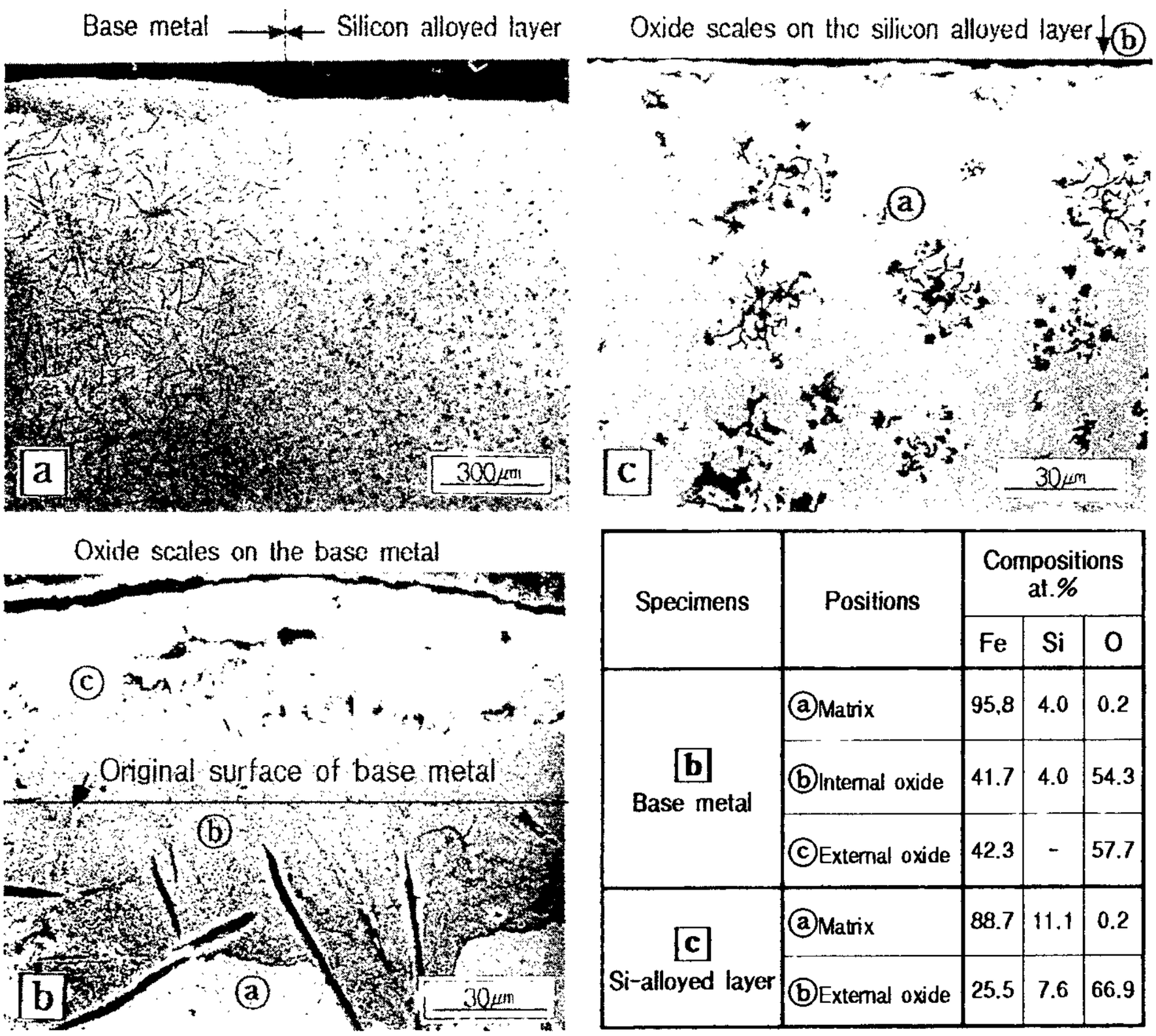

Specimens	Positions	Compositions at.%		
		Fe	Si	O
[b] Base metal	ⓐMatrix	95.8	4.0	0.2
	ⓑInternal oxide	41.7	4.0	54.3
	ⓒExternal oxide	42.3	-	57.7
[c] Si-alloyed layer	ⓐMatrix	88.7	11.1	0.2
	ⓑExternal oxide	25.5	7.6	66.9

Fig. 8. Scanning electron micrographs and chemical compositions of oxide scales formed on GS50 at 1098K for 18.0Ks in the air. (a) low magnification of silicon alloyed layer, (b) high magnification of oxide scale on the gray cast iron and (c) on the silicon alloyed layer.

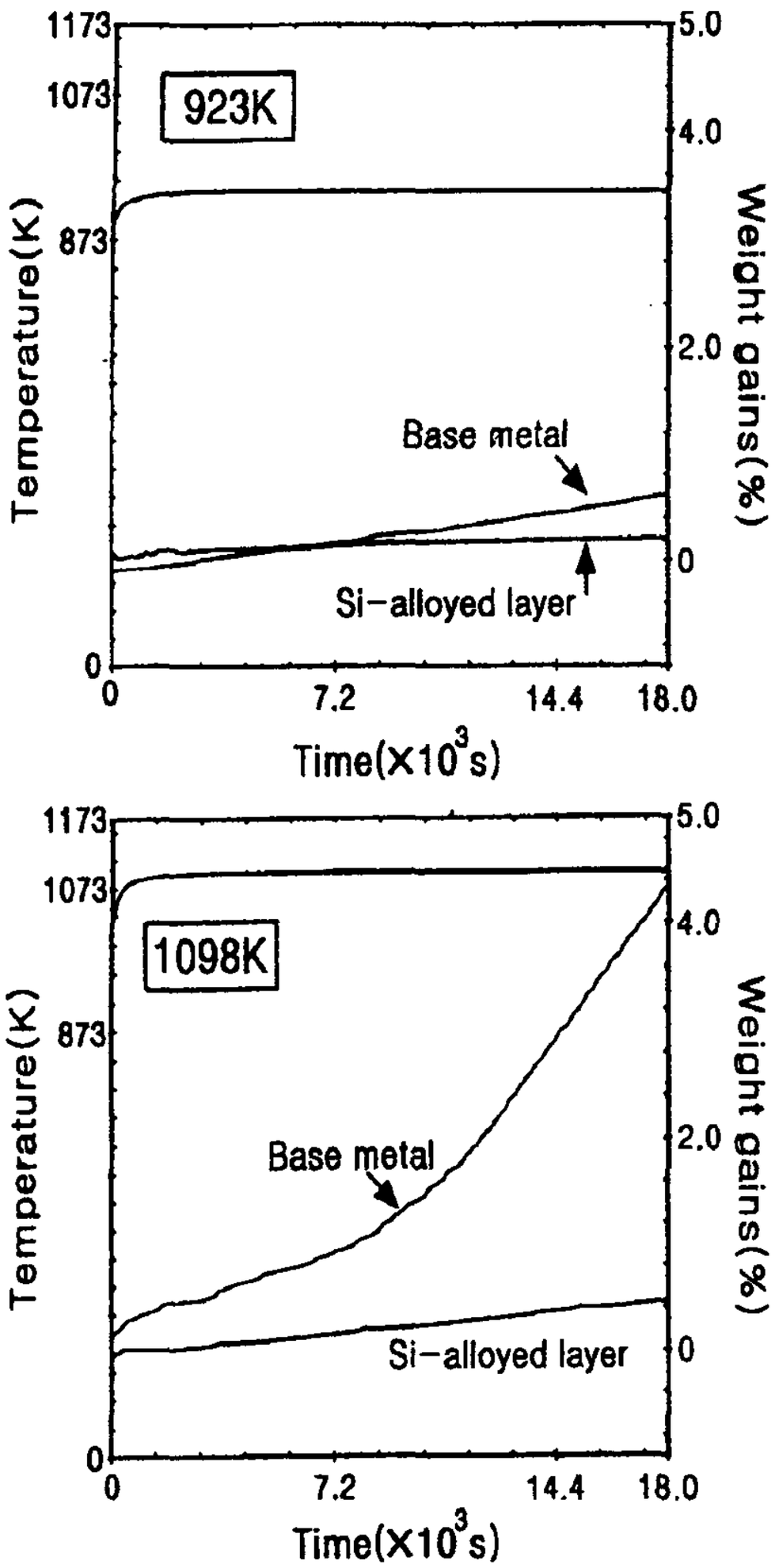

Fig. 9. Thermogravimetric analysis of base metal and silicon alloyed layer at 923K and 1098K for 18.0ks in the air.

internal scales was about 60~70 μm. EPMA analysis for [Fe], [Si] and [O] indicated that the composition of the external scale was 42.3at.%Fe-57.7 at.%O with no silicon and that of the internal scale was 41.7at.%Fe-54.3at.%O-4.0at.%Si which had similar silicon content to the matrix. However, in the silicon alloyed layer as shown in Fig. 8c, only tight and thin external scale with the thickness of 3~5 μm was formed and the composition was 88.8at.%Fe-0.2at.%O-11.0at.%Si.

Fig. 9 shows the result of TGA in the specimens taken from the silicon alloyed layer in GS50 and oxidized in the air at 923K and 1098K up to 18.0ks. The weight gain of the base metal and the silicon alloyed layer were 0.6% and 0.2% at 923K and 4.3% and 0.42% at 1098K, respectively. Silicon alloyed layer showed significant improvement in oxidation resistance especially at high temperature level. From these results, it was confirmed that high temperatrure oxidation resistant layer can be produced on the cast iron surface due to the formation of tight silicon oxide layer.

4. Conclusion

A commercial flake graphite cast iron substrate was coated with silicon powder by low pressure plasma spraying and was irradiated with a CO_2 laser to produce the high-temperature oxidation resistant silicon alloyed layer.

The melt depth and width of bead increased by the silicon coat in comparision with those of an as-blasted cast iron due to the increasing absorption efficiency of laser beam. The microstructure of bead section of alloyed with silicon consisted of FZ and HAZ, but did not show the ledeburite zone. The solidification microstructure of silicon alloyed layer contained the fine chunky like graphites with 20 μm in size and network structure of Fe_5Si_3 precipitated in the eutectic cell boundary.

When the base metal was high temperature oxidized in the air, the oxide scale consisted of the porous external scale layer (42.3at.%Fe-57.7at.%O) grown outside from the original surface and internal scale layer (41.7at.%Fe-54.3at.%O-4.0at.%Si) grown along the flake graphites in the matrix. On the other hand, oxide scale on the silicon alloyed layer only showed dense external scale layer (88.8at.%Fe-0.2at.%O-11.0at.% Si). This observation indicated that the formation of oxide scale at high temperature was severely inhibited by the surface alloying of silicon. In addition, the weight gain in the silicon alloyed layer was about 1/3 at 923K and about 1/10 at 1098K compared to that of the base metal. Therefore, high temperature oxidation resistance was significantly improved by the surface alloying of silicon.

The microhardness of silicon alloyed bead section

showed irregular distribution in the range of MHV 300 to 1100. Post-heat treatment at 1223K for 18.0ks in vacuum and furnace cooling, however, decreased it to smooth distribution of MHV 300 to 500.

Acknowledgement

The authors wish to thanks to Mr. R. Nagayama, technical assistant in the Joining and Welding Research Institute of Osaka University, who assisted to plasma spraying.

References

[1] W. M. Steen, "Laser Material Processing", (Springer-Verlag, 1991), 172.
[2] H. E. Cline and T. R. Anthony, J. of Applied Physics, 48 (1977) 3895.
[3] C. W. Draper and J. M. Poate, Int. Metal Review, 30 (1985) 85.
[4] T. Chande and J. Mazumder, Metall. Trans. 14B (1983) 181.
[5] C. W. Draper, Applied Optics, 20 (1981) 3093.
[6] R. Elliott, "Cast Iron Technology", (Butterworths London, 1989) 102-109.
[7] M. Tsujikawa *et al*, Imono, 64 (1992) 613.
[8] NIKKEI MECHANICAL, 468 (1995) 24.
[9] F. D. Seaman and D. S. Gnanamuthu, Metal Prog. (1975) 67.
[10] H. W. Bergermann, Surface Engineering, 1 (1985) 137.
[11] W. Amende, Konstruieren und giessen, 20 (1995) 26.
[12] A. L. Norbury and E. Morgan, JISI, 174, (1979) 17.
[13] "Metals Handbook, Vol. 1", 10th edn, ASM, 1990 85.
[14] W. H. White, L. P. Rice and A. R. Elsea, AFS Trans., 59 (1951) 337.
[15] W. F. Smith, "Structure and Properties of Engineering Alloys", (McGraw-Hill,Inc. 1981) 358.
[16] H. I. Park, S. G. Kim, B. W. Lee, J. of Korean Foundrymen's Soc., 17 (1997) 293.
[17] Y. Takata *et al*, Imono, 60 (1985) 332.
[18] G. J. Bruck, J. of Metal, (Feburary 1987) 10.
[19] Y. Tanaka and T. Hiraoka, Imono, 62 (1990) 412.
[20] H. Umehara, Bulletin of the JIM, 27 (1988) 766.
[21] R. W. Heine, AFS Trans., 94 (1986) 391.
[22] H. Tamura, J. of the JWS, 38 (1969) 117.
[23] J. Tartera, AFS Int. Cast Metals J., 5 (1980) 7
[24] S. V. Subramanian, D. A. R. Kay and G. R. Purdy, AFS Trans., (1982) 589.
[25] I. Minkoff, "The Physical Metallurgy of Cast Iron", (John Wiley and Sons Ltd., 1983) 91.
[26] J. F. Janowak, R. B. Gundlach, AFS Trans., (1982) 847.